

Introducing the Condor Array Telescope. 1. Motivation, Configuration, and Performance

KENNETH M. LANZETTA,¹ STEFAN GROMOLL,² MICHAEL M. SHARA,³ STEPHEN BERG,¹ DAVID VALLS-GABAUD,⁴
FREDERICK M. WALTER,¹ AND JOHN K. WEBB⁵

¹*Department of Physics and Astronomy, Stony Brook University, Stony Brook, NY 11794-3800, USA*

²*Amazon Web Services, 410 Terry Ave. N, Seattle, WA 98109, USA*

³*Department of Astrophysics, American Museum of Natural History, Central Park West at 79th St., New York, NY 10024-5192, USA*

⁴*Observatoire de Paris, LERMA, CNRS, 61 Avenue de l'Observatoire, 75014 Paris, FRANCE*

⁵*Clare Hall, University of Cambridge, Herschel Road, Cambridge CB3 9AL, UNITED KINGDOM*

(Received October 29, 2022; Accepted December 29, 2022)

Submitted to Publications of the Astronomical Society of the Pacific

ABSTRACT

The “Condor Array Telescope” or “Condor” is a high-performance “array telescope” comprised of six apochromatic refracting telescopes of objective diameter 180 mm, each equipped with a large-format, very low-read-noise ($\approx 1.2 e^-$), very rapid-read-time (< 1 s) CMOS camera. Condor is located at a very dark astronomical site in the southwest corner of New Mexico, at the Dark Sky New Mexico observatory near Animas, roughly midway between (and more than 150 km from either) Tucson and El Paso. Condor enjoys a wide field of view ($2.29 \times 1.53 \text{ deg}^2$ or 3.50 deg^2), is optimized for measuring *both* point sources *and* extended, very low-surface-brightness features, and for broad-band images can operate at a cadence of 60 s (or even less) while remaining sky-noise limited with a duty cycle near 100%. In its normal mode of operation, Condor obtains broad-band exposures of exposure time 60 s over dwell times spanning dozens or hundreds of hours. In this way, Condor builds up deep, sensitive images while simultaneously monitoring tens or hundreds of thousands of point sources per field at a cadence of 60 s. Condor is also equipped with diffraction gratings and with a set of He II 468.6 nm, [O III] 500.7 nm, He I 587.5 nm, H α 656.3 nm, [N II] 658.4 nm, and [S II] 671.6 nm narrow-band filters, allowing it to address a variety of broad- and narrow-band science issues. Given its unique capabilities, Condor can access regions of “astronomical discovery space” that have never before been studied. Here we introduce Condor and describe various aspects of its performance.

Keywords: Automated telescopes (121), Telescopes (1689), Automatic patrol telescopes (122), Astronomical detectors (84)

1. INTRODUCTION

In the hierarchical or “bottom-up” scenario of galaxy formation, galaxies are formed as gas cools and condenses into dark-matter halos, which are themselves formed via hierarchical merging and accretion of sub-galactic fragments. Numerical simulations of structure formation in a dark-energy-dominated, cold-dark-matter (Λ CDM) Universe predict that the virialized regions surrounding massive galaxies should be filled with such fragments, which should leave signs of their merging and accretion histories in the form of tidal tails, streams, and debris. Yet deep images of nearby galaxies fail to detect satellite galaxies or their tidal effects at anywhere near the density of the fragments predicted by the simulations. This discrepancy is known as the “substructure” or “missing satellites” or “missing outskirts” problem (e.g. Klypin et al. 1999; Merritt et al. 2020).

A possible solution to the problem is that the satellite galaxies and their tidal effects *are* there, but at a surface brightness below the sensitivity of deep images obtained by reflecting telescopes. The surface-brightness sensitivity of a reflecting telescope is ultimately limited by systematic effects produced by light that is diffracted by the secondary mirror and then reflected and scattered by the optical assembly. Perhaps reflecting telescopes are simply unsuitable

for detecting the very low-surface-brightness light of satellite galaxies and their tidal effects? (Refracting telescopes are limited by different systematic effects related to scattering within and between the lenses.)

This possibility motivated [Abraham & van Dokkum \(2014\)](#), hereafter AvD) to pioneer a new type of astronomical telescope optimized for detecting extended, very low-surface-brightness features. Specifically, AvD combined eight off-the-shelf Canon telephoto lenses of focal length 400 mm and focal ratio $f/2.8$ (hence objective diameter 143 mm) with eight off-the-shelf Santa Barbara Imaging Group STF-8300M CCD cameras and a robotic telescope mount to form an eight-element “telephoto array,” which they named “Dragonfly.” Because the lenses are not subject to the same systematic effects that limit reflecting telescopes, the array is sensitive to low surface brightnesses. Dragonfly is located in the Northern Hemisphere, in New Mexico, and has since been upgraded to 48 lenses.

Dragonfly has been used to identify previously unknown very low-surface-brightness “ultra-diffuse” galaxies in the Coma Cluster, which have sizes comparable to the size of the Milky Way but contain only 0.1–1% of the stars ([Merritt et al. 2016b](#)). The array has also been used to study the stellar halo around the spiral galaxy M101 ([van Dokkum et al. 2014](#)), to identify ultra-diffuse galaxies in the field surrounding M101 ([Merritt et al. 2014](#)) and in a group containing the elliptical galaxy NGC 5485 ([Merritt et al. 2016b](#)), and to study the stellar halos of various nearby galaxies ([Merritt et al. 2016a](#); [Gilhuly et al. 2022](#)).

A similar telescope was constructed by [Spitler et al. \(2019\)](#), who combined 10 telephoto lenses with 10 CCD cameras to form a 10-element telephoto array, which they named “Huntsman” and which is located in the Southern Hemisphere, at the Siding Spring Observatory in Australia.

Several years ago, we became interested in the possibilities of astronomical telescopes optimized for detecting extended, very low-surface-brightness features, and our subsequent musings on some of the issues involved led us to note the following:

- Dragonfly is not well suited to measuring point sources. The plate scale of its detectors is $2.8 \text{ arcsec pix}^{-1}$, hence point sources are significantly undersampled under seeing conditions typical of good astronomical sites (say FWHM $\approx 1.2 \text{ arcsec}$) and so are susceptible to blending and intrapixel sensitivity variations (e.g. [Kavaldjiev & Ninkov 2001](#)). Further, the Canon lenses are not designed to be diffraction limited, and indeed AvD measured Strehl ratios of their lenses ranging from 0.2 to 0.8, with an average of only 0.4. While point sources are not central to the scientific agenda of AvD, this is nevertheless a limitation of the array.
- The Canon lenses used by Dragonfly suffer significant vignetting, which limits possibilities of upgrading to larger-format detectors. Over the $18 \times 14 \text{ mm}^2$ size of the Dragonfly detectors, AvD measured vignetting at the field edges of 20%. But the “image circle” (i.e. the diameter over which the intensity exceeds 60% of the central intensity) of the lenses is only $\approx 25 \text{ mm}$, and over a $36 \times 24 \text{ mm}^2$ detector (a popular “full-frame” format for commercial detectors), the lenses suffer vignetting at the field edge of 60%. Hence the lenses can just barely illuminate a full-frame detector and certainly not a larger detector.
- Due to rapidly developing commercial CMOS technology, very large-format ($\approx 150 \text{ Mpix}$), very rapid-read-time ($< 1 \text{ s}$), very low-read-noise ($\approx 1 \text{ e}^-$) CMOS cameras were at the time of our deliberations just becoming available. Whereas exposures with CCD detectors must be relatively long (say $\approx 600 \text{ s}$) to remain sky-noise limited and to maintain high duty cycle, exposures with these new CMOS detectors could be much shorter, offering exciting possibilities of very rapid cadence (say $\approx 60 \text{ s}$ or even shorter) observations.

With these considerations in mind, we began to conceive the prototype element of an “array telescope” that was to be constructed using off-the-shelf, diffraction-limited refracting telescopes of longer focal length (hence finer plate scale) than Dragonfly and incorporating the new off-the-shelf CMOS cameras. It was also clear to us that the possibilities of very rapid cadence observations opened up by the new CMOS detectors were similar to those of other array telescopes designed for time-domain astronomy that are currently under construction or in advanced planning stages, including the Large-Array Survey Telescope or LAST ([Ofek & Ben-Ami 2020](#)) and the Argus Array ([Law et al. 2022](#)). So in this sense, these other array telescopes offered other relevant points of comparison.

In mid summer 2019, we were awarded NSF Advanced Technologies and Instrumentation (ATI) funding for proposal 1910001, “Concept Feasibility Study for a High-Performance Telescope Array.” The proposal outlined a plan to combine off-the-shelf refracting telescopes with off-the-shelf CMOS cameras to construct an array telescope to be located at a very dark astronomical site in the Southern Hemisphere, at the El Sauce Observatory in the Rio Hurtado Valley of Chile, about 15 km from Gemini and LSST. We dubbed the nascent telescope the “Condor Array Telescope”

or simply “Condor,” referencing the Andean condor that is a national symbol of Chile and a significant character of the mythologies of various Andean cultures.

But this funding was awarded just months before the Covid-19 pandemic struck in early 2020, and by the time we began to assemble components of the telescope, it had become clear to us that it would not be possible to deploy the telescope to Chile anytime soon. Accordingly, in early autumn 2020, we began to search for an alternate (perhaps temporary) site for Condor in the continental USA—one that could be reached by car from our base of operations in New York (as flying was frowned upon near the peak of Covid-19). We eventually selected a very dark astronomical site in the southwest corner of New Mexico, at the Dark Sky New Mexico observatory near Animas, roughly midway between (and more than 150 km from either) Tucson and El Paso. Over the period early winter 2020 through early summer 2021, we deployed and commissioned Condor to the Dark Sky New Mexico observatory. In its new setting, its name perhaps evokes the California condor, whose native range as recently as 500 years ago likely included New Mexico (Gander et al. 1931).

Condor shares an objective of very low-surface-brightness sensitivity with Dragonfly and Huntsman; but Condor differs from these other telescopes in several significant ways, in terms of motivation, configuration, and mode of operation. Here we introduce Condor and describe various aspects of its performance. The organization of this manuscript is as follows: In § 2 we describe the motivation, in § 3 we describe the configuration, and in § 4 we describe the performance. In § 5 we discuss the mode of operation, which plays an important role in setting Condor apart from other telescopes. We present a summary and conclusions in § 6.

2. MOTIVATION

Telephoto arrays like Dragonfly and Huntsman and array telescopes like Condor operate by building up deep, sensitive images over time, staring at one spot on the sky and acquiring many individual exposures over dwell times that might span dozens or even hundreds of hours. Subsequent analysis forms deep, sensitive images by coadding the individual exposures. For Dragonfly, individual exposure times are typically 600 s, and dwell times can reach many dozens of hours or up to around 100 hours.

Our thinking with respect to Condor was that if we were going to stare at one spot on the sky and acquire many individual exposures over dwell times spanning dozens or hundreds of hours, then we might as well at the same time monitor point sources near that spot on the sky at an interesting cadence. This immediately led to the key design decisions that (1) Condor should be optimized for measuring *both* point sources *and* extended, very low-surface-brightness features and (2) Condor should operate at a rapid cadence. Optimizing for point sources requires diffraction-limited optics and a finer plate scale and hence longer focal length than Dragonfly or Huntsman; these requirements (together with the requirement of very low-surface-brightness sensitivity) dictated apochromatic refracting telescopes. Operating at a rapid cadence requires a low detector read noise and a rapid detector read time; these requirements dictated CMOS detectors. Hence early on, we knew that Condor must be constructed of apochromatic refracting telescopes equipped with CMOS cameras.

For Condor to simultaneously monitor point sources at a rapid cadence and build up deep, sensitive images by acquiring many individual exposures requires that the individual exposures must be sky-noise limited. This obviously involves some interplay between cadence, telescope aperture, filter bandpass, plate scale, and detector read noise. We explored different combinations of telescopes, filters, and detectors, considering telescope objective diameters in the range 150 through 200 mm. Cost was also a significant driver here, as a given light-collecting ability might be achieved by using more smaller telescopes (which implies more cameras, filters, and other peripherals and a correspondingly higher data rate) or fewer larger telescopes (which implies fewer cameras, filters, and other peripherals and a correspondingly lower data rate). We identified a sweet spot at an objective diameter of 180 mm, where for a given light-collecting ability the combined cost of the telescopes plus cameras, filters, and other expensive peripherals was minimized.

There is also an interplay between cadence and the depth of each individual exposure, with an obvious trade off between shorter, shallower individual exposures (with a correspondingly higher data rate) or longer, deeper individual exposures (with a correspondingly lower data rate). We eventually settled on a primary cadence of 60 seconds and a primary filter with a luminance bandpass. Given a telescope of objective diameter 180 mm and a low-read-noise, rapid-read-time CMOS camera, observations obtained under such a configuration would be sky-noise limited even under very dark conditions and would operate at a duty cycle near 100%. And combining six such telescopes (which is what would fit within the allotted budget), each individual summed (luminance-bandpass) exposure would reach a

depth of ≈ 21 mag, which is well matched to the limiting depth of the Gaia catalog (Gaia Collaboration et al. 2017, 2018).

Further, our thinking with respect to Condor was that an instrument optimized for very low-surface-brightness sensitivity could fruitfully be directed at obtaining narrow- as well as broad-band images. Remarkably, most of the sky has *never* been imaged in the prominent emission lines of astrophysics. The nearly-completed WHAM Sky Survey (e.g. Haffner et al. 2011) used a Fabry-Perot spectrometer to scan the entire sky in H α 656.3, but at an angular resolution of only 1 deg, while the IPHAS and VPHAS+ surveys (Wright 2016) achieved higher resolution but covered less than 10% of the sky. Deep imaging observations in He II 468.6, [O III] 500.7, and [S II] 671.6 of ≈ 100 nearby galaxies have been used to detect supernova remnants, Wolf-Rayet stars, and planetary nebulae, respectively, but together these observations cover just a few percent of the sky. And the state-of-the-art SIGNALS survey (Rousseau-Nepton et al. 2019) expects to obtain sensitive observations toward ≈ 100 nearby galaxies using an imaging Fourier transform spectrograph on the CFHT, but it too will cover only a tiny portion of the sky. Because most of the sky remains mostly unknown in most emission lines, here the potential for the discovery of new phenomena is high. This led to another key design decision that (3) Condor should be equipped with a variety of narrow-band filters tuned to some of the prominent emission lines of astrophysics.

Our ultimate design of the prototype element of Condor satisfied each of the three key design decisions and was eventually made manifest in the instrument deployed to New Mexico. This design may be summarized as follows:

- Condor is comprised of six apochromatic refracting telescopes of objective diameter 180 mm and effective focal length 907 mm, which results in a much finer plate scale than Dragonfly or Huntsman. It can obtain nearly Nyquist-sampled images at a good astronomical site and hence, unlike Dragonfly or Huntsman, is optimized for measuring *both* point sources *and* extended, very low-surface-brightness features.
- Condor is equipped with large-format (9576×6388), very low-read-noise ($\approx 1.2 e^-$), very rapid-read-time (< 1 s) CMOS cameras, in contrast to the CCD cameras of Dragonfly and Huntsman. It enjoys a wide field of view ($2.29 \times 1.53 \text{ deg}^2$ or 3.50 deg^2) and for broad-band images can operate at a cadence of 60 s (or even less) while remaining sky-noise limited with a duty cycle of nearly 100%.
- Like Dragonfly and Huntsman, Condor is equipped with a set of Sloan g' , r' , and i' broad-band filters (one each per telescope). But Condor is also equipped with luminance filters and diffraction gratings (one each per telescope) and a set of He II 468.6 nm, [O III] 500.7 nm, He I 587.5 nm, H α 656.3 nm, [N II] 658.4 nm, and [S II] 671.6 nm narrow-band filters (one per telescope), allowing it to address a variety of broad- and narrow-band science issues.
- Condor is equipped with a direct-drive mount that can slew anywhere on the sky in under 3.5 s, allowing it to efficiently intersperse calibration observations between science observations throughout the course of each night.

Given its unique capabilities, Condor can access regions of “astronomical discovery space” (Harwit 1984) that have never before been studied. We describe details of the configuration in the following section.

3. CONFIGURATION

3.1. Telescopes

The prototype element of Condor is comprised of six Telescope Engineering Company (TEC) 180 mm-diameter f/7 refracting telescopes of focal length 1260 mm. The telescopes feature diffraction-limited, apochromatic, oil-spaced, triplet objective lenses with multi-layer coatings on all surfaces and a CaF₂ middle element. Each optical assembly sits within a lightweight aluminum tube coated with an anti-reflection coating, and each tube assembly contains custom-designed and -fabricated sharp-edged baffles throughout the interior. The baffles of two of the telescopes are coated with a standard black paint, while the baffles of four of the telescopes are coated with Singularity Black carbon-nanotube paint, thus allowing for the possibility of assessing the performance of very black carbon-nanotube paint on the telescope baffles.

3.2. Focal-Reducing Field Correctors

Each TEC telescope is equipped with an Astro-Physics (A-P) 0.72x QUADTCC-TEC180 four-element telecompressor corrector. These correctors when used with the TEC 180 mm-diameter telescopes yield an effective focal length of 907

mm and an effective focal ratio of $f/5.0$. The effective focal ratio of the six telescopes together, considered as a single telescope, is $f/2.0$.

3.3. CMOS Cameras

Each TEC telescope is equipped with a ZWO ASI6200MM monochrome CMOS camera, which is based on the large-format Sony IMX455 back-illuminated detector. The cameras feature USB3.0 interfaces and 256 MB DDR3 caches. The cameras use Peltier coolers to cool the detectors to as much as 40 C below the ambient temperature. Specifications of the CMOS camera detectors are summarized in Table 1.

Table 1: CMOS Camera Detector Specifications

Detector size	$36 \times 24 \text{ mm}^2$
Detector format	9576×6388
Pixel size	$3.76 \text{ }\mu\text{m}$
Maximum full-well capacity	51 ke^-
Read noise	1.3 to 3.5 e^-
ADC bits	16
Peak quantum efficiency	80%
Maximum full-resolution frame rate	3.2 fps

3.4. Filter Wheels

Each TEC telescope is equipped with a ZWO EFW 7/2" seven-position filter wheel. Each filter wheel is capable of holding seven 2-inch round filters.

3.5. Filters and Diffraction Gratings

Each TEC telescope is equipped with (1) a Sloan g' filter, (2) a Sloan r' filter, (3) a Sloan i' filter, (4) a luminance filter, and (5) a narrow-band filter, each manufactured by Chroma Technology Corp. The six narrow-band filters are tuned to emission lines of (1) He II 468.6 nm, (2) [O III] 500.7 nm, (3) He I 587.5 nm, (4) $H\alpha$ 656.3 nm, (5) [N II] 658.4 nm, and (6) [S II] 671.6 nm. The six narrow-band filters have widths of $\approx 4 \text{ nm}$. Typical response functions of the various filters (as measured by the manufacturer) are shown in Figure 1. The peak transmission of each filter approaches 100%. The Sloan i' and luminance filters exhibit infrared leak, which is more significant for the luminance filters.

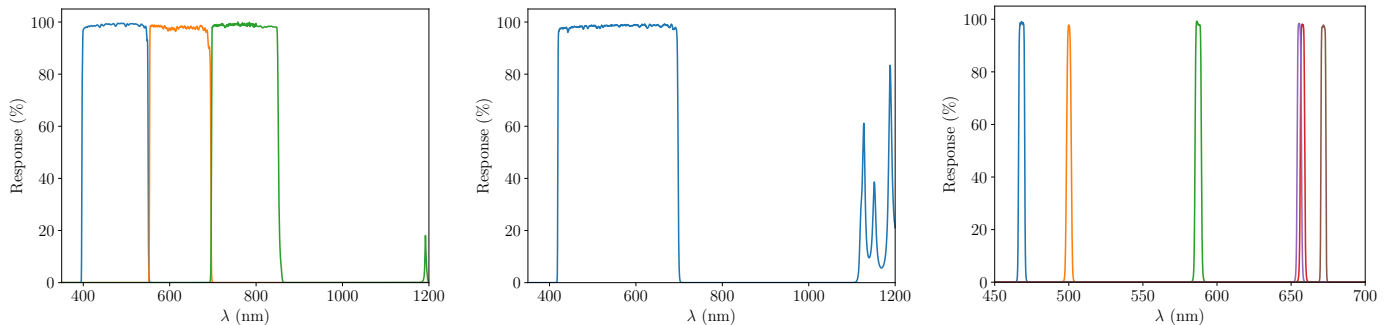


Figure 1. Typical response functions of the various filters (as measured by manufacturer): (a, left) the Sloan g' (blue), r' (orange), and i' (green) filters, (b, middle) the luminance filter, and (c, right) the He II 468.6 nm (blue), [O III] 500.7 nm (orange), He I 587.5 nm (green), $H\alpha$ 656.3 nm (purple), [N II] 658.4 nm (red), and [S II] 671.6 nm (brown) filters.

Each TEC telescope is also equipped with a Star Analyzer 200 diffraction grating distributed by Field Tested Systems, LLC. The gratings are ruled at $100 \text{ lines mm}^{-1}$ and blazed in first-order at a wavelength of 550 nm and provide a resolution of $R \equiv \lambda/\Delta\lambda \approx 200$. The dispersion directions of the various diffraction gratings are oriented in such a way that they are rotated with respect to one another, which can significantly aid in untangling the various overlapping spectra of the various sources in the field of view.

3.6. *Focusers*

Each TEC telescope is equipped with an Optec TCF-Leo low-profile motorized focuser. The focusers have a step size of $0.08 \mu\text{m}$ and a maximum range of travel of $\approx 9 \text{ mm}$.

3.7. *Dust Covers*

Each TEC telescope is equipped with an Optec Alnitak motorized dust cover.

3.8. *Mount*

The six TEC telescopes are mounted onto a Planewave L-600 half-fork mount with equatorial wedge. The mount features direct-drive motors and precision encoders on each axis and slew speeds of up to 50 deg s^{-1} and is not subject to backlash or periodic error. The telescopes are attached to the mount using a custom-designed and -fabricated bracket that allows the telescopes to be independently collimated with respect to each other.

3.9. *Site*

Condor is located at a very dark astronomical site in the southwest corner of New Mexico, at the Dark Sky New Mexico observatory near Animas, roughly midway between (and more than 100 miles from either) Tucson and El Paso, at an elevation of 1341 m. Details of the site are summarized in Table 2.

Table 2: Details of the Site

Latitude	31.94638° N
Longitude	108.89755° W
Elevation	1341 m

The telescope is housed in an observatory building with a roll-off roof. Images of Condor in its observatory building at the Dark Sky New Mexico observatory are shown in Figure 2.



Figure 2. Images of Condor in its observatory building with a roll-off roof at the Dark Sky New Mexico observatory near Animas, New Mexico. In both images, the dust covers are closed.

3.10. *Control and Acquisition Computers*

The CMOS cameras, filter wheels, focusers, dust covers, mount, and observatory roof are controlled by and data are acquired by eight Raspberry Pi 4 “control and acquisition” computers running Ubuntu 20.04, which are located in a control room adjacent to the telescope. Each Raspberry Pi 4 computer is equipped with a 128 GB SATA III solid-state drive connected via USB3.0, and each computer and drive assembly is mounted into a custom-designed and -fabricated 3-D-printed enclosure, and the eight computer and drive enclosures are mounted into a server rack. The server rack

also contains a router, a 1 TB solid-state drive, and environmental monitor, an IP power distribution unit, a power distribution unit, and three focus controller hubs. The 1 TB solid-state drive is used to stage data, the environmental monitor is used to monitor temperature and humidity and the state of the observatory roof, the IP power distribution unit is used to remotely cycle power to the computers and other peripherals, and the focus controllers are used to control the focusers. An image of the Raspberry Pi 4 computers and the server rack is shown in Figure 3.

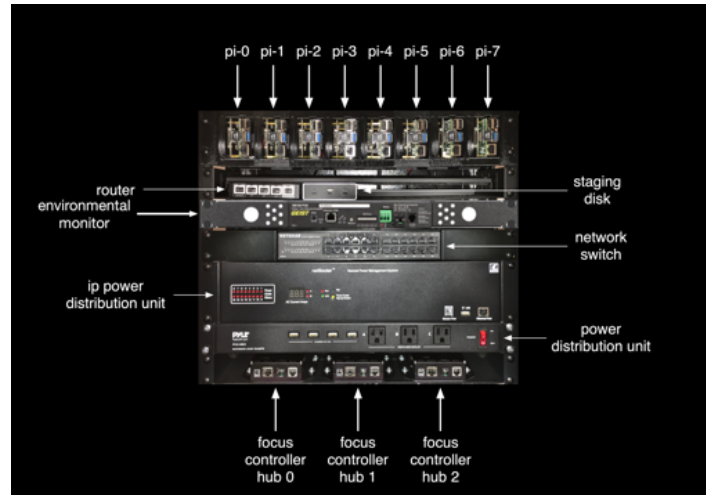


Figure 3. Image of Raspberry Pi 4 computers and server rack. Server rack contains eight computer and drive enclosures, a router, a 1 TB solid-state drive, and environmental monitor, an IP power distribution unit, a power distribution unit, and three focus controller hubs.

Each CMOS camera is connected to a Raspberry Pi 4 computer via USB3.0. The other peripherals (filter wheels, focusers, dust covers, mount, and observatory roof) are connected to Raspberry Pi 4 computers via USB2.0 or Ethernet. In operation, one Raspberry Pi 4 computer acts as a “sequencer” and sends instructions to other Raspberry Pi 4 computers, which in turn send instructions to the various peripherals. As images are acquired, they are temporarily staged to the 128 GB solid state drives and then promptly transferred to storage and analysis computers on the campus of Stony Brook University (described in § 3.11) and from there to storage and analysis computers at the American Museum of Natural History. The Raspberry Pi 4 computers continuously report information (related to status of the observations, status of the peripherals, status of the computers themselves, and weather) to a database running on one of the storage and analysis computers; these communications are cached locally, ensuring that they are not lost in the event of a disruption to the storage and analysis computers or a loss of Internet connectivity. Current and predicted weather is continuously monitored via the Tomorrow.io weather API; these weather observations are used to assess local conditions bearing on whether the observatory roof should be opened or closed and are recorded for later use in science analysis.

3.11. *Storage and Analysis Computers*

Data acquired by Condor are stored on and analyzed by six Dell PowerEdge R720xd “storage and analysis” computers running Ubuntu 20.04, which are located at the Data Center on the campus of Stony Brook University. Each Dell R720xd computer is equipped with one or more solid-state drives, which are used to store the operating system and local scratch space; several high-capacity (14 to 18 TB) hard disk drives, which are used to store data; and 768 GB DDR3 memory. The various Dell R720xd computers each run MinIO, which is an open-source object storage system that is functionally compatible with AWS S3, and data acquired by Condor are ultimately stored under MinIO clusters. The various MinIO clusters are configured for a factor two redundancy, and the system is robust against loss of drives and loss of computers. One Dell R720xd computer hosts the Condor web site and runs a PostgreSQL database, and all six Dell R720xd computers participate in the analysis of data.

4. PERFORMANCE

Condor obtained its first-light image on March 7, 2021 and has since acquired thousands of hours of observations. Here we describe the performance based on analysis of some of these observations.

4.1. Characteristics of the CMOS Detectors

Here we describe characteristics of the Sony IMX455 detectors used in the ZWO ASI6200MM monochrome CMOS cameras.

4.1.1. Nominal Gain, Read Noise, Full-Well Capacity, and Dynamic Range

Various properties of the CMOS detectors (as specified by the manufacturer) are shown in Figure 4 as functions of the “gain setting,” including nominal full-well capacity, gain, dynamic range, and read noise. It is apparent from Figure 4 that there are two obvious choices of gain setting: a “low-gain” setting of 0 yields a nominal gain of $0.8 \text{ e}^- \text{ ADU}^{-1}$, a nominal full-well capacity of 51 ke^- , a nominal read noise of 3.5 e^- , and a dynamic range of just under 14 stops, while a “high-gain” setting of 100 yields a nominal gain of $0.27 \text{ e}^- \text{ ADU}^{-1}$, a nominal full-well capacity of 19 ke^- , a nominal read noise of 1.5 e^- , and a dynamic range of again just under 14 stops. In practice, we obtain observations at the high-gain setting of 100.

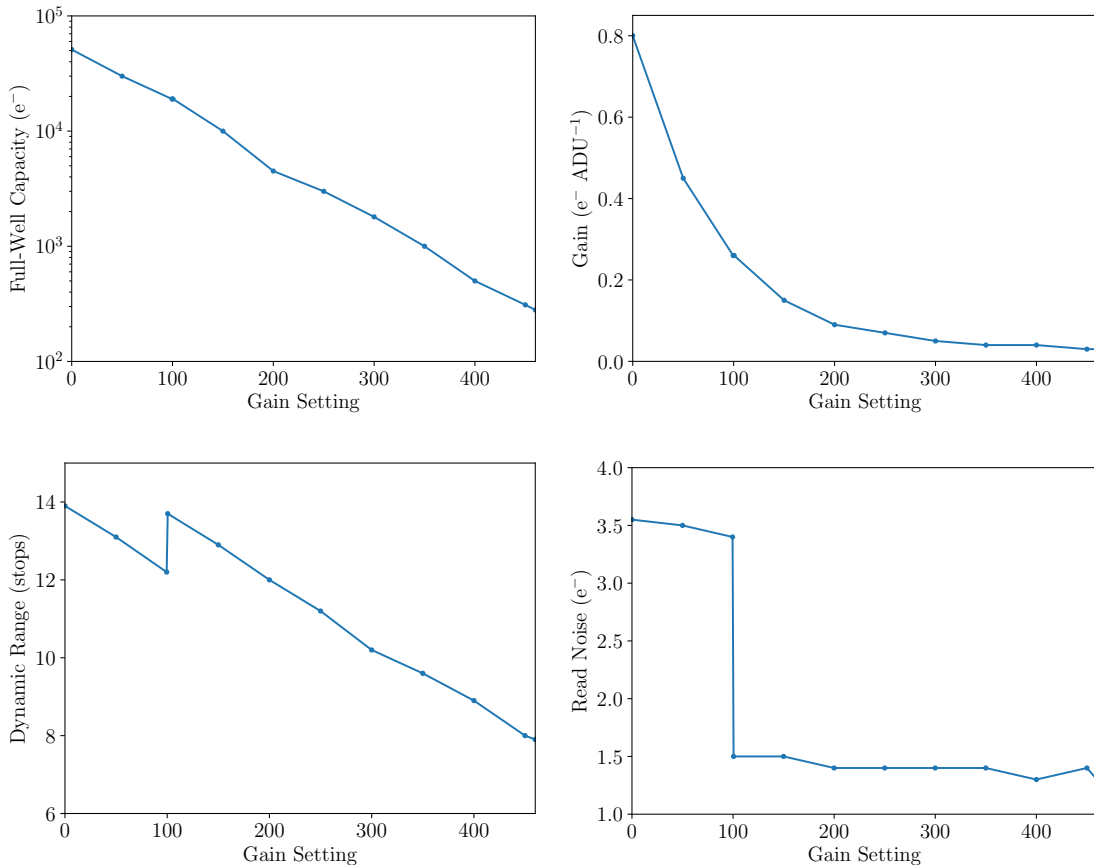


Figure 4. Various properties of CMOS detectors (as specified by manufacturer): (a, upper left) full-well capacity versus gain setting, (b, upper right) gain versus gain setting, (c, lower left) dynamic range versus gain setting, and (d, lower right) read noise versus gain setting. In practice, we obtain observations at the “high-gain” setting of 100.

4.1.2. Bias and Pixel Noise

Condor obtains frequent (typically daily) sequences of 500 zero-exposure “bias images” of each CMOS detector in order to assess bias and pixel noise. From these sequences of bias images, we produce “master bias images” that

consist of two planes: one plane contains the pixel-by-pixel median of the sequence, and the other plane contains the pixel-by-pixel standard deviation about the median of the sequence. We take the median plane to be the pixel-by-pixel bias level, and we take the standard deviation plane to be the pixel-by-pixel pixel noise level. In practice, we obtain observations at a bias setting of 10, which yields a nominal bias level of 100 ADU. Adopting the nominal gain $0.27 \text{ e}^- \text{ ADU}^{-1}$ described in § 4.1.1, this corresponds to a nominal bias level in electron units of 27 e^- .

Pixel-by-pixel comparisons of the bias levels of four master bias images obtained a day apart, a week apart, and nearly six months apart are shown in Figure 5. From Figure 5, it is apparent that: (1) Most pixels ($> 99\%$) always exhibit a bias level very close to 100 ADU. (2) Some pixels ($\lesssim 1\%$) exhibit a bias level less than or greater than 100 ADU in a way that is stable versus time in the sense that the bias levels of these pixels are highly correlated with near unit slope between various pairs of master bias images. And (3) a small fraction ($\lesssim 0.002\%$) of pixels exhibit a bias level very close to 100 ADU after previously exhibiting a bias level less than or greater than 100 ADU—or vice versa—in such a way that the bias levels of these pixels are not highly correlated between various pairs of master bias images. We find it notable that the fraction of pixels with bias levels that are not highly correlated—even nearly six months apart—is $\lesssim 0.002\%$. The various standard deviations between the various pairs of images of Figure 5 are $\approx 0.47 \text{ ADU}$. Similar results are obtained for different combinations of master bias images (acquired up to and beyond a year apart) and for master bias images of different detectors. We conclude that the pixel-by-pixel bias levels of the CMOS detectors are very stable over long periods of time.

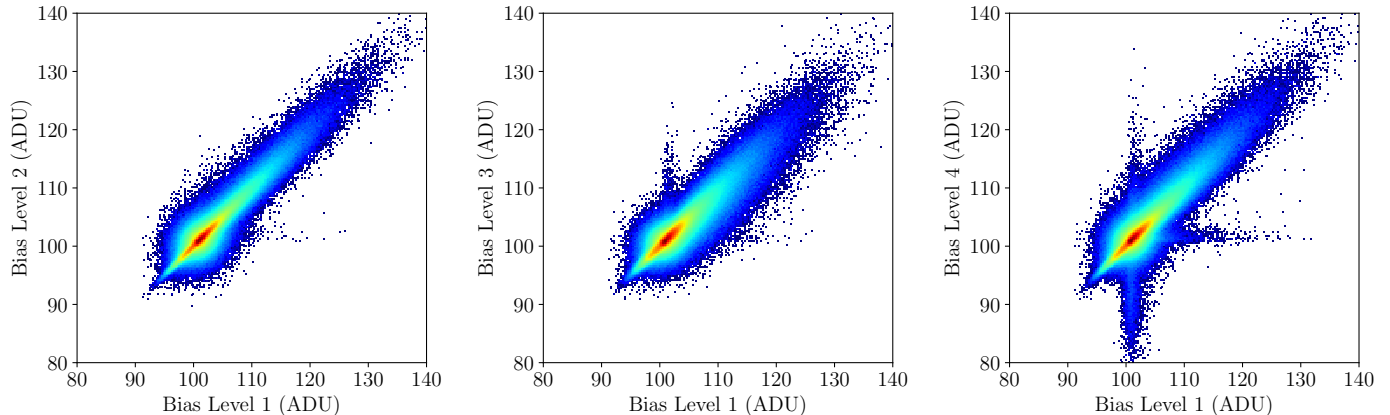


Figure 5. Pixel-by-pixel comparisons of bias levels of “master bias” images 1 (obtained on May 27, 2022), 2 (obtained on May 26, 2022), 3 (obtained on May 20, 2022), and 4 (obtained on November 22, 2021), all obtained by the same detector of telescope 4. (All comparisons are with respect to master bias image 1.) Displays are logarithmic heat maps, with red representing largest values and blue representing smallest values.

Pixel-by-pixel comparisons of the standard deviations of four master bias images obtained a day apart, a week apart, and nearly six months apart are shown in Figure 6. From Figure 6 it is apparent that: (1) Most pixels ($> 90\%$) always exhibit a standard deviation very close to 4.3 ADU. (2) Some pixels ($\sim 10\%$) exhibit a standard deviation greater than 4.3 ADU in a way that is stable versus time in the sense that the standard deviations of these pixels are highly correlated between various pairs of master bias images. (3) A small fraction ($\lesssim 0.001\%$) of pixels exhibit a standard deviation very close to 4.3 ADU after previously exhibiting a standard deviation greater than 4.3 ADU—or vice versa—in such a way that the standard deviations of these pixels are not highly correlated between various pairs of master bias images. And (4) a small fraction ($\lesssim 0.001\%$) of pixels exhibit a standard deviation greater than 4.3 ADU after previously exhibiting a standard deviation close to 4.3 ADU in such a way that the standard deviations of these pixels are highly correlated between various pairs of master bias images but with a slope greater than unity. We find it notable that the fraction of pixels with standard deviations that are not highly correlated or that are highly correlated with a slope greater than unity—even nearly six months apart—is $\lesssim 0.001\%$. The various standard deviations between the various pairs of images of Figure 6 are $\approx 0.61 \text{ ADU}$. Similar results are obtained for different combinations of master bias images (acquired up to and beyond a year apart) and for master bias images of different

detectors. We conclude that the pixel-by-pixel standard deviations of the CMOS detectors are very stable over long periods of time.

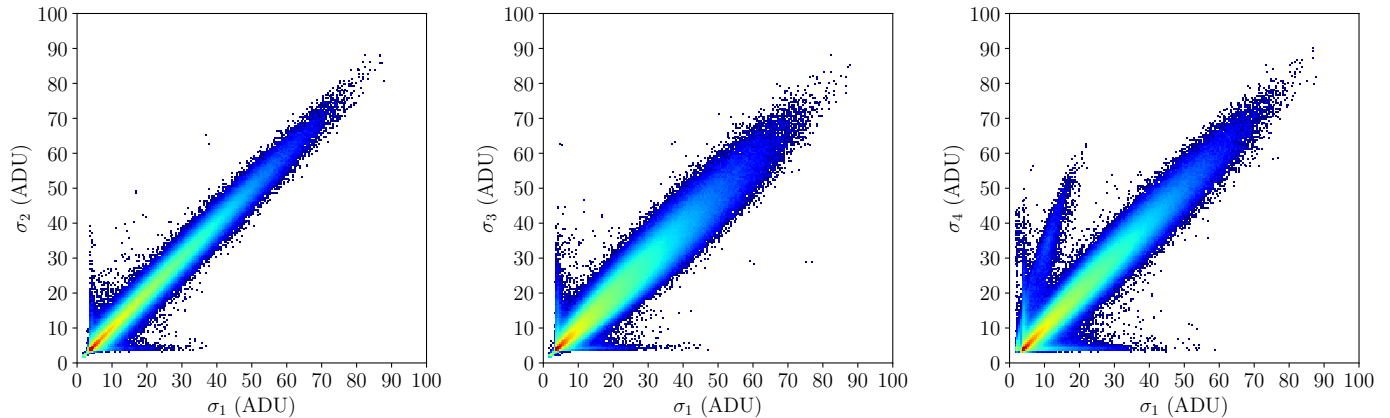


Figure 6. Pixel-by-pixel comparisons of standard deviations of “master bias” images 1 (obtained on on May 27, 2022), 2 (obtained on May 26, 2022), 3 (obtained on May 20, 2022) and 4 (obtained on November 22, 2021), all obtained by the same detector of telescope 4. (All comparisons are with respect to master bias image 1.) Displays are logarithmic heat maps, with red representing largest values and blue representing smallest values.

The distribution of the pixel-by-pixel standard deviations of one of the master bias images from Figure 5 is shown in Figure 7, expressed in electron units adopting the nominal gain $0.27 \text{ e}^- \text{ ADU}^{-1}$ described in § 4.1.1 and displayed on linear and logarithmic scales. From Figure 7 it is apparent that (1) the lowest pixel noise levels are $\approx 0.8 \text{ e}^-$ and (2) the distribution of the pixel noise levels has a long tail that extends to nearly 25 e^- . The mode and median of the pixel noise level distribution pixel are each 1.2 e^- , which is significantly lower than nominal value 1.5 e^- of the read noise described in § 4.1.1. Similar results are obtained for different master bias images and for master bias images of different detectors.

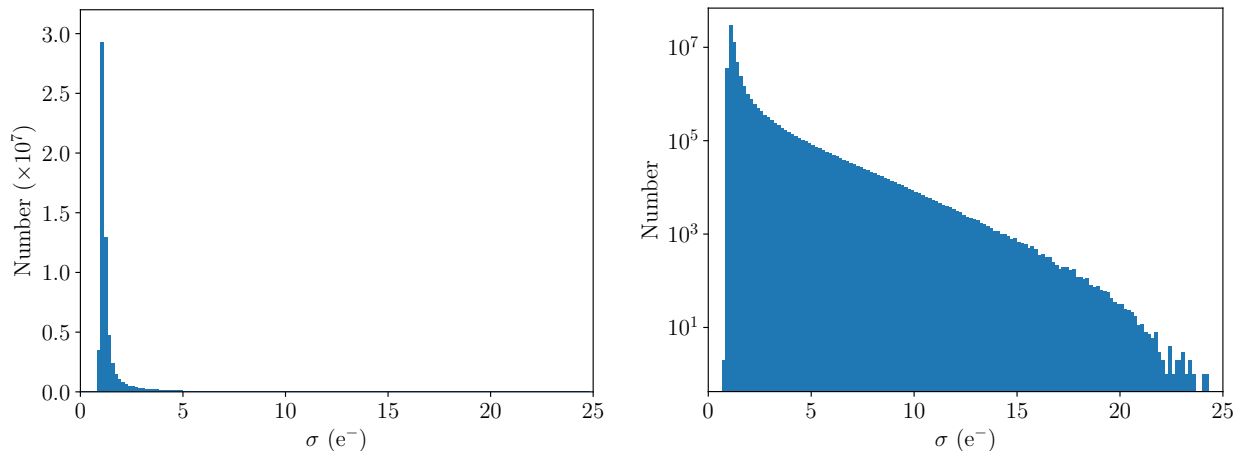


Figure 7. Distribution of pixel-by-pixel standard deviations of master bias image 1 from Figure 3, expressed in electron units and shown on (a, left) a linear scale and (b, right) a logarithmic scale. Mode and median of the distribution are each 1.2 e^- . Bin widths are 0.2 e^- .

It is well known that CMOS detectors exhibit “random telegraph noise” (RTN), which is evident as a long tail in the distribution of pixel noise levels of bias or dark images that extends to many times (up to 10 or 100) the median of the distribution (e.g. [Chao et al. 2019](#)). This RTN is a phenomenon that results from capture and release of electrons

by defects in the gate oxide of the detector. We attribute the long tail of the distribution of Figure 7b to RTN, or in other words, we postulate that the pixels that exhibit a pixel noise level significantly in excess of the median $1.2 e^-$ of the distribution result from RTN. Roughly 12% of the pixels of the master bias image from which Figure 7 was constructed exhibit a pixel noise level in excess of $2 e^-$, which drops to 6% in excess of $3 e^-$, 2% in excess of $5 e^-$, and 0.3% in excess of $10 e^-$.

But we see no reason to make a conceptual distinction between pixels that exhibit “read noise” and pixels that exhibit “random telegraph noise.” The pixel noise level distribution of Figure 5 is unimodal rather than bimodal, and we believe that any such distinction would be arbitrary. Accordingly, we say that the “read noise” of the detector is the value $1.2 e^-$ of the median (and mode) of the distribution but that some small fraction of pixels exhibit pixel noise levels significantly in excess of the read noise. Because we characterize the pixel noise level of each pixel individually and because the pixel noise level is very stable (as discussed above), the RTN has little effect in practice. Pixels that are significantly affected by RTN can be included into any processing weighted by their associated pixel noise levels with no detrimental effect, or such pixels can be identified and excluded from processing (say for purposes of visual display).

4.1.3. Gain

We determined the gain of each CMOS detector by measuring pixel-to-pixel fluctuations in flattened quotients of pairs of images of the twilight sky. (See § 4.5 for a brief discussion of our field flattening and background subtraction techniques.) We found a gain of $0.26 e^- \text{ ADU}^{-1}$ for each CMOS detector, which is very close to the nominal gain $0.27 e^- \text{ ADU}^{-1}$ described in § 4.1.1.

4.1.4. Linearity

We assessed the linearity of each CMOS detector by measuring the gain of the detector (as described in § 4.1.3) as a function of the “illumination” (or the average signal level across the detector) in flattened quotients of pairs of images of the twilight sky with similar values of illumination. We found that the gain increases by $\approx 0.38\%$ as the illumination varies from 54,000 to 57,000 ADU. An example of gain versus illumination is shown in Figure 8. We defer a more detailed assessment of linearity until later.

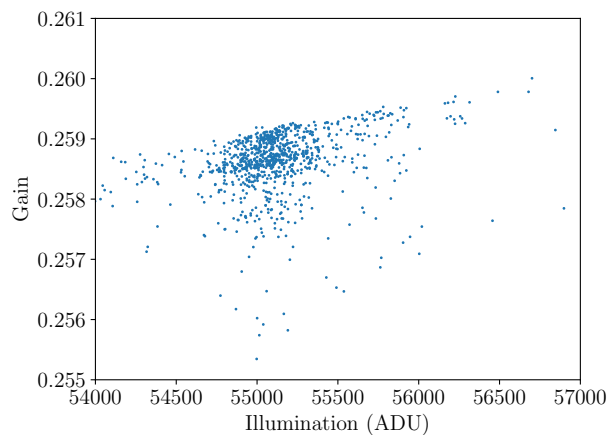


Figure 8. Gain versus illumination measured from flattened quotients of pairs of images of twilight sky obtained by telescope 4 in spring 2022. Here “illumination” is average signal level across detector. Measured points trace out an upper envelope that indicates that gain increases by $\approx 0.38\%$ as illumination varies from 54,000 to 57,000 ADU. Points that deviate below predominant trend of gain versus illumination arise due to contributions to the pixel-to-pixel fluctuations of twilight-sky quotients in excess of photon statistics (like clouds). We take upper envelope as indicative of relationship between gain and illumination.

4.1.5. Dark Current

We determined the dark current of each CMOS detector by the measuring the mean values of bias-subtracted dark images of exposure 3600 s. We found a dark current of typically $1.4 \times 10^{-3} e^- \text{ s}^{-1} \text{ pix}^{-1}$ for each CMOS detector at a detector temperature of $\approx -12 \text{ C}$. There are no obvious significant patterns or structures in the dark images.

4.1.6. Image Persistence

We searched for evidence of “image persistence”—or the tendency of some CMOS detectors to capture and retain charge when illumination levels are high and to then gradually release this charge over time (Karpov et al. 2021)—by comparing back-to-back dithered images of bright stars. The same portions of two 100 s dithered images of Vega obtained 11 s apart are shown in Figure 9. There is no evidence of persistence of the image of Vega from the first exposure to the second exposure. Similar results are obtained for other images of bright stars and for images of bright stars obtained by the other telescopes. We conclude that images obtained by the CMOS detectors are not significantly affected by image persistence.

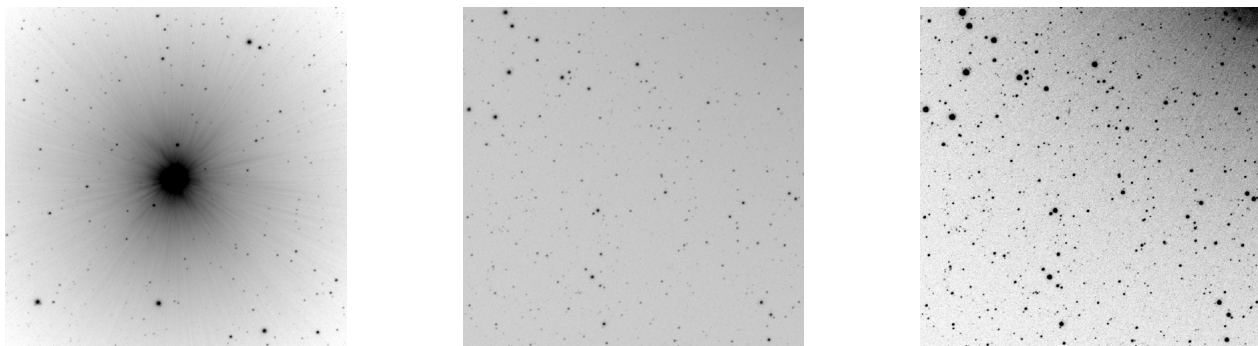


Figure 9. Images of Vega and vicinity obtained by telescope 2 on June 7, 2022: (*a, left*) image obtained at 08:23:19 UTC with exposure of 100 s on logarithmic stretch, (*b, center*) image obtained at 08:25:10 UTC with exposure of 100 s on logarithmic stretch, (*c, right*) same image as in *b*, but on linear stretch. In all cases, a $1000 \times 1000 \text{ pix}^2$ portion of the image is shown, centered on the location of Vega in the first image. There is no evidence of persistence of the image of Vega from the first exposure to the second exposure.

4.1.7. Cosmic Ray Events

We assessed the incidence of cosmic ray events by processing images through MaxiMask (Paillassa et al. 2020), which is a convolutional neural network that detects contaminants in astronomical images. Applied to a 60-s exposure, this processing identifies typically 20,000 events that are classified as cosmic ray events, each extending over typically 12 pixels and in total affecting $\approx 0.4\%$ of the pixels comprising the image. But these events involve very little charge (typically $\lesssim 100 e^-$ each), and no pixels are ever close to saturated by these events, and these events are always very localized. The incidence of these events is much higher than is expected for cosmic ray events, and we are uncertain as to the nature of these events and whether few, some, many, or most of these events are indeed produced by cosmic rays. But this processing nevertheless establishes an upper limit to the incidence of cosmic ray events. We conclude that images obtained by the CMOS detectors are not significantly affected by cosmic ray events.

4.1.8. Cosmetic Defects

We found the CMOS detectors to be notably unaffected by the various “cosmetic” defects typical of CCD detectors, including hot and dark pixels and charge bleeding from saturated stars.

4.1.9. Summary

Several of us have extensive experience working with CCD detectors dating back many decades. Our overall impression is that the Sony IMX455 back-illuminated detector performs superbly. We are particularly impressed with the very large format, the very low read noise, the low dark current, the 16-bit ADC, the high quantum efficiency, the very rapid read time, the long-term stability, and the absence of cosmetic defects. We believe that CMOS detectors should and will soon replace CCD detectors in most or all astronomical applications.

4.2. Plate Scale and Field of View

Considering the $3.76 \mu\text{m}$ pixel size of the 9576×6388 format Sony IMX455 detector together with the nominal effective focal length 907 mm of the TEC 180 mm telescope with the A-P 0.72x four-element telecompressor corrector yields a nominal plate scale of $0.86 \text{ arcsec pixel}^{-1}$ and a nominal field of view $2.29 \times 1.53 \text{ deg}^2$. The measured values after astrometric calibration are very close to the nominal values. (See § 4.4 for a brief discussion of our astrometric calibration techniques.) The solid angle subtended by the field of view is 3.50 deg^2 . Details of the plate scale and field of view are summarized in Table 3.

Table 3: Details of Plate Scale and Field of View

Plate scale	$0.86 \text{ arcsec pix}^{-1}$
Field of view	$2.29 \times 1.53 \text{ deg}^2$
Solid angle subtended by field of view	3.50 deg^2

The Rayleigh limit of a 180 mm-diameter aperture ranges from $\approx 0.5 \text{ arcsec}$ at wavelength $\lambda = 350 \text{ nm}$ to $\approx 1.0 \text{ arcsec}$ at $\lambda = 700 \text{ nm}$, which when convolved with a seeing profile of width, say, $\text{FWHM} = 1.2 \text{ arcsec}$ typical of a good astronomical site yields a point-spread function (PSF) of width ranging from $\text{FWHM} \approx 1.3 \text{ arcsec}$ at $\lambda = 350 \text{ nm}$ through $\text{FWHM} \approx 1.6 \text{ arcsec}$ at $\lambda = 700 \text{ nm}$. The 0.86 arcsec plate scale of the telescope Nyquist samples a PSF of $\text{FWHM} \approx 1.7 \text{ arcsec}$, hence Condor slightly undersamples the PSF under seeing conditions typical of a good astronomical site, by a factor ranging from as much $\approx 25\%$ at $\lambda = 350 \text{ nm}$ through as little as $\approx 6\%$ at $\lambda = 700 \text{ nm}$. We conclude that Condor can obtain nearly Nyquist-sampled images at a good astronomical site.

4.3. Detector Uniformity and Vignetting

An image of the twilight sky obtained with one of the six telescopes is shown in Figure 10. From Figure 10 it is apparent that: (1) The detector response is very uniform over the field of view, and the detector exhibits no obvious blemishes or cosmetic flaws. (As is expected, several out-of-focus dust motes are clearly visible in the image of Figure 10.) (2) The image circle is well centered on the detector, which indicates that the optical beam is well collimated. And (3) the detector is nearly but not quite fully illuminated by the image circle, with vignetting evident at the corners of the image. Similar results are obtained for other twilight images and for twilight images obtained by the other telescopes.

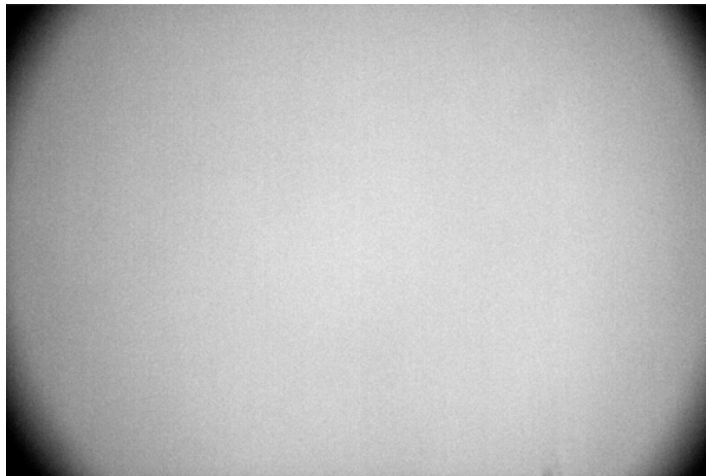


Figure 10. Image of twilight sky obtained by telescope 4 near dawn on May 30, 2022. Several out-of-focus dust motes are clearly visible in the image.

A diagonal cut across the image of Figure 10 running from the upper left corner to the lower right corner is shown in Figure 11. From Figure 11 it is apparent that the illumination of the detector is very flat across most of the field of

view, with vignetting again evident at the corners of the image. The maximum vignetting at the very corners of the image reaches $\approx 15\%$. Similar results are obtained for other twilight images and for twilight images obtained by the other telescopes.

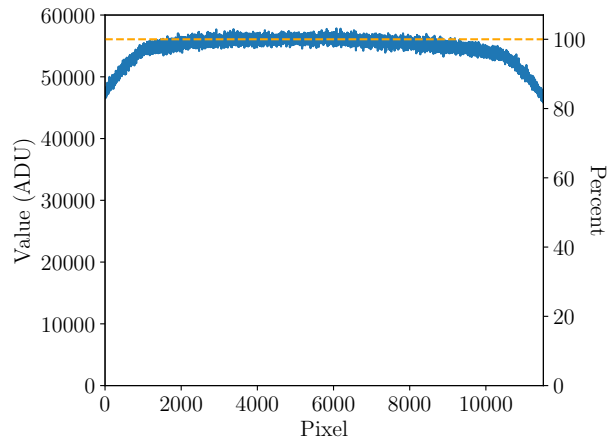


Figure 11. Diagonal cut across image of Figure 9 running from upper left corner to lower right corner. Dashed orange line is set to peak mean value near center of image.

4.4. Astrometric Calibration

Details of the astrometric calibration of Condor images will be described elsewhere, but here we present a brief summary of our procedures and results.

Accurate astrometric calibration is crucial for all of the science objectives of Condor. Yet determining an accurate astrometric calibration over the wide field of view of Condor is not straightforward, especially in the presence of geometric distortions and field curvature at the corners of the images. Accordingly, we developed a technique of measuring astrometric calibration that is appropriate to Condor images. Briefly, the technique proceeds as follows: First, we start with a science image for which bias subtraction and field flattening and background subtraction have already been performed. Next, we process the image through SExtractor (Bertin & Arnouts 1996a), which is a program that identifies sources in astronomical images. This processing produces a list of pixel coordinates of sources detected in the image. Next, we query the Gaia DR3 catalog (Gaia Collaboration et al. 2017, 2018, 2021) to obtain a list of sources in the field, noting in particular the celestial coordinates and proper motions of the sources. Next, we fit for parameters of the affine transformation that best matches the pixel and celestial coordinates (corrected for proper motions) of a subset of the sources, and we construct a list of matched pixel and celestial coordinates of the sources. Finally, we fit for parameters of a higher-order model that best matches the pixel and celestial coordinates, taking as parameters the affine transformation parameters and the coefficients of a seventh-order geometric distortion polynomial including radial terms, in the “TPV” projection. (The TPV projection is similar to the TAN projection described by Calabretta & Greisen 2002 but includes a seventh-order geometric distortion polynomial.)

By applying this technique, we consistently obtain an astrometric calibration with systematic differences between the transformed pixel and celestial coordinates of $\lesssim 0.1$ arcsec.

4.5. Field Flattening and Background Subtraction

Details of the field flattening and background subtraction of Condor images will be described elsewhere, but here we present a brief summary of our procedures and results.

Field flattening and background subtraction are critical to many of the science objectives of Condor. Yet there are no obvious flat sources of illumination to which Condor could be pointed to produce field-flattening calibration images. We experimented with producing “sky flat” images by median combining unregistered science images (after scaling to account for difference in background level). But we note two very significant problems with this approach: (1) the night sky is itself not flat, and (2) photon noise in a sky flat image can never be made insignificant in comparison to photon noise in the (combined) science images, because the number of photons recorded by the sky flat image grows only in direct proportion to the number of photons recorded by the science images.

Instead, we have developed a technique of field flattening and background subtraction that is based on forming a quotient with a twilight image. Briefly, the technique proceeds as follows: First, the science image is divided by a twilight image (obtained by the same telescope with the same detector). This quotient is devoid of all instrumental effects (including all telescope and detector effects) but contains the signatures of the (different and unknown) sky backgrounds of the science and twilight images. Next, the quotient is fitted by a high-order (typically eighth-order) two-dimensional polynomial, rejecting regions around sources present in the science image. This polynomial fit accounts for the backgrounds of both the science and twilight images. Finally, the polynomial fit is subtracted from the quotient. This sequence of steps produces a version of the science image that is simultaneously corrected for field flattening and background subtraction.

By experimenting with pairs of twilight images (i.e. by substituting another twilight image for the science image), we found that we are able to carry out field flattening and background subtraction to within fundamental physical limitations. In particular, we found that the residuals of the quotients after the polynomials are subtracted result from (1) rapidly-varying (i.e. with times scales less than ≈ 10 s) stochastic fluctuations of the atmosphere on scales of several hundred pixels and (2) photon statistics on scales of one pixel. We used this technique, for example, to determine the gain of each CMOS detector by measuring photon statistics on scales of one pixel of pairs of twilight images, as described in § 4.1.3.

4.6. Photometric Calibration

Details of the photometric calibration of Condor images will be presented elsewhere, but here we present a brief summary of our procedures and results.

Exquisite photometric calibration is not critical to many of the science objectives of Condor. Accordingly, our current efforts have concentrated on obtaining an approximate photometric calibration suitable for quantifying sensitivity and for identifying variable and transient sources. Briefly, the technique proceeds as follows: First, we start with science images for which bias subtraction, astrometric calibration, and field flattening and background subtraction have been performed. Next, we query the Gaia DR3 catalog (Gaia Collaboration et al. 2017, 2018, 2021) to obtain a list of sources in the field, noting in particular the celestial coordinates and g' magnitudes of the sources. Next, we use aperture photometry techniques to measure brightnesses of sources in the list of sources, excluding very bright or very faint sources. Finally, we compare the measured brightnesses to the g' magnitudes across the ensemble to derive a rough photometric calibration.

The distributions of the “photometric calibration” (i.e. the energy flux density that corresponds to 1 ADU s^{-1}) and the “magnitude zero point” (i.e. the g' magnitude that corresponds to 1 ADU s^{-1}) measured for a large number of images obtained through the luminance filter are shown in Figure 12. From Figure 12 it is apparent that under the clearest conditions ever experienced by Condor, the photometric calibration is $\approx 3.5 \mu\text{Jy ADU}^{-1} \text{ s}$ and the magnitude zero point m_0 is $m_0 \approx 22.7$ through the luminance filter. Measurements of the photometric calibration and magnitude zero point through other filters are given in Appendix A.

4.7. Image Quality and Point-Spread Function

An image of Vega obtained by one telescope is shown in Figure 13. This image demonstrates that the Condor PSF is exceptionally clean and that the only apparent features of the PSF are (1) a very faint reflection visible to the lower left of the star in the left panel and (2) very low-level “spikes” that emanate radially from the star (which are more easily seen in the right panel). Following AvD, we tentatively attribute these spikes to diffraction from striae in the glass elements and lattice imperfections in the crystalline CaF_2 elements of the lenses. The left panel of Figure 13 may be directly compared to Figure 8 of AvD, which is a similar image of Venus on a logarithmic stretch over a scale of 50 arcmin. (But we note that Venus is, of course, not a point source.) The Condor image appears substantially cleaner than the Dragonfly image, and the Condor image does not show the multiple reflections, “ghosts,” and halos evident in the Dragonfly image. Similar results are obtained for other images of Vega (and other bright sources) and for images of Vega (and other bright sources) obtained by the other telescopes.

The Condor PSF pieced together from the image of Figure 13 and other similar images of exposure times 0.1, 1, 10, and 100 s is shown in Figure 14. In Figure 14, the vertical axis gives surface brightness μ_{PSF} of a zero-magnitude source in units mag arcsec^{-2} , and the horizontal axis gives angular distance r in units arcsec on a logarithmic scale. In Figure 14, the PSF on scales $r > 10$ arcsec was estimated by determining the median values within circular annuli centered on Vega. The median values in ADU units were converted to surface brightness units using the photometric

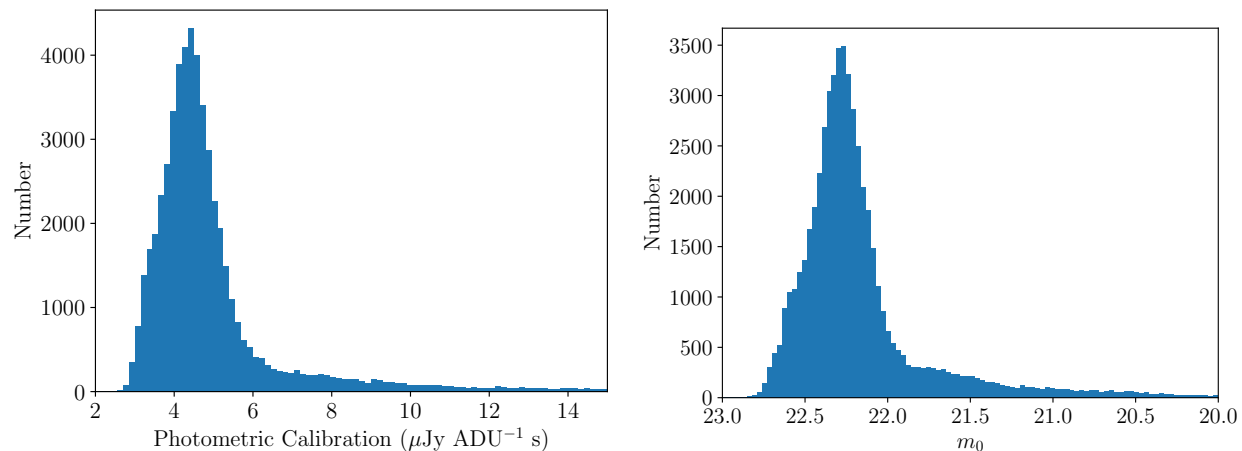


Figure 12. Distributions of (*a, left*) “photometric calibration” (i.e. energy flux density that corresponds to 1 ADU s^{-1}) and “magnitude zero point” m_0 (i.e. g' magnitude that corresponds to 1 ADU s^{-1}) of images obtained through luminance filter over time interval stretching from April 21, 2021 through June 19, 2022. Bin width of left panel is $1.5 \mu\text{Jy ADU}^{-1} \text{ s}$, and bin width of right panel is 0.03 mag.

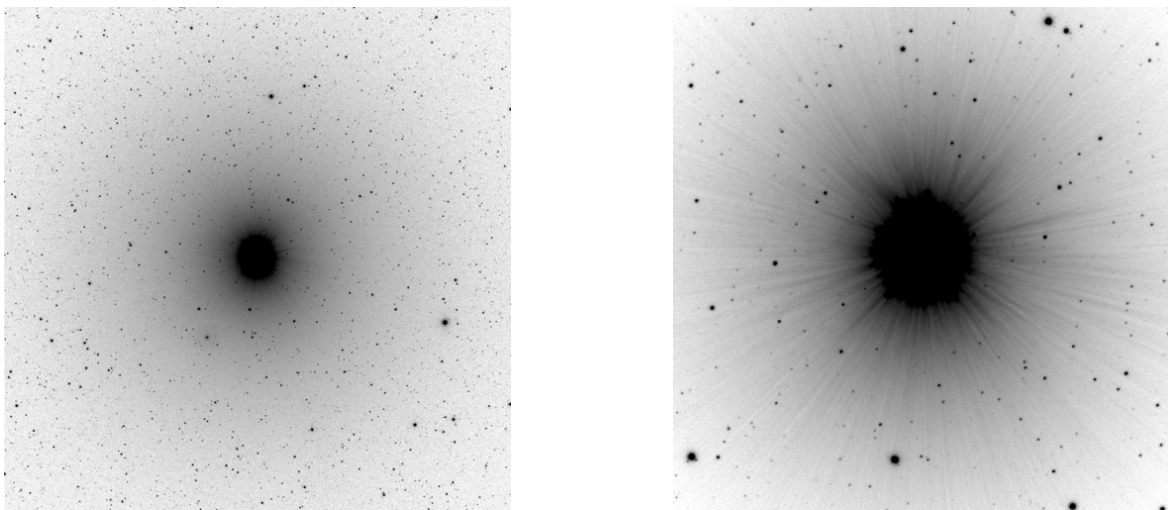


Figure 13. Image of Vega obtained by telescope 2 on June 7, 2022 with an exposure time of 100 s on a logarithmic stretch over a scale of (*a, left*) 50 arcmin on a side and (*b, right*) 12.5 arcmin on side. This image demonstrates that the Condor PSF is exceptionally clean and that the only apparent features of the PSF are (1) a very faint reflection visible to the lower left of the star in the left panel and (2) very low-level “spikes” that emanate radially from the star (which are more easily seen in the right panel). Following AvD, we tentatively attribute these spikes to diffraction from striae in the glass elements and lattice imperfections in the crystalline CaF_2 elements of the lenses. The left panel may be directly compared to Figure 8 of AvD, which shows a similar image of Venus obtained by Dragonfly on a logarithmic stretch over a scale of 50 arcmin.

calibration described in § 4.6, but otherwise these values were not scaled in any way. This is appropriate because Vega is the primary photometric standard. On scales $r < 10 \text{ arcsec}$ the image of Vega was saturated even in the 0.1 s exposure, so the PSF was estimated by determining the median values within circular annuli of a fainter star. Figure 14 also shows the Dragonfly PSF from Liu et al. (2022). The two PSFs are very similar on scales $r \lesssim 50 \text{ arcsec}$ but appear to deviate on scales $r \gtrsim 50 \text{ arcsec}$. But it is important to note that: (1) the Condor PSF on scales $r \lesssim 5 \text{ arcsec}$

is set by seeing conditions and (2) both the Condor and Dragonfly PSFs on scales $r \gtrsim 10$ arcsec depend on weather and atmospheric conditions. We defer a detailed comparison between the Condor and Dragonfly PSFs until later.

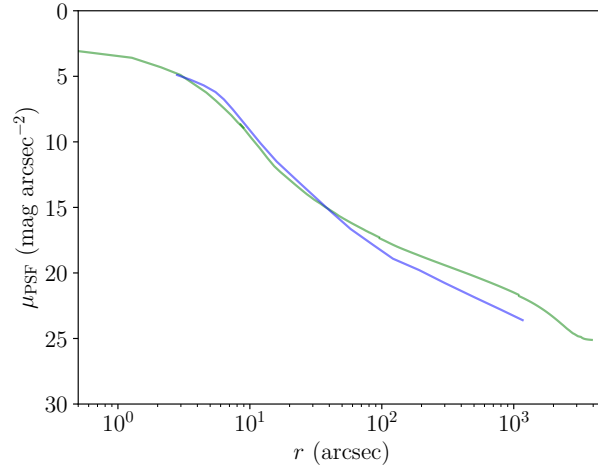


Figure 14. Condor PSF (green) determined from image of Figure 13 and other similar images of exposure times 0.1, 1, 10, and 100 s. Vertical axis gives surface brightness μ_{PSF} of a zero-magnitude source in units mag arcsec^{-2} , and horizontal axis gives angular distance r in units arcsec on a logarithmic scale. Plot also shows Dragonfly PSF (blue) from Liu et al. (2022). The two PSFs are similar on scales $r \lesssim 50$ arcsec but appear to deviate on scales $r \gtrsim 50$ arcsec. But note that: (1) Condor PSF on scales $r \lesssim 5$ arcsec is set by seeing conditions and (2) both Condor and Dragonfly PSFs on scales $r \gtrsim 10$ arcsec depend on weather and atmospheric conditions.

The distribution of the “image quality” FWHM of a large number of images obtained through the luminance filter are show in Figure 15. We define the “image quality” FWHM of an image to be the FWHM of the central core of the autocorrelation function of the image. We found through experimentation that the FWHM of the central core of the autocorrelation function of an image is ≈ 2 times the typical FWHM of point sources in the image. Hence the image quality FWHM is an easily-measured statistic that characterizes the typical FWHM of point sources in the image. We note that the typical FWHM of point sources in the image is set by a combination of seeing, focus, tracking errors, and field curvature (in the sense that focus may not be completely uniform across the field). Hence the distribution of Figure 15 represents the sum of these effects. In the months immediately following first light, when methods of controlling focus, tracking errors, and field curvature were still being developed, these effects contributed significantly to image quality. But by several months later, when these effects were better controlled, image quality was set primarily by seeing. The mode of the image quality FWHM distribution is 1.6 arcsec, and the median of the distribution is 2.0 arcsec. Because Condor Nyquist samples a PSF of FWHM ≈ 1.7 arcsec (as described in § 4.2), its configuration is well matched to the typical image quality obtained at the Dark Sky New Mexico observatory site.

4.8. Night-Sky Background

The distributions of the “night-sky background rate” (in units $e^- s^{-1} \text{pix}^{-1}$) and the “night-sky surface brightness” μ_{sky} (in units mag arcsec^{-2}) measured for a large number of images obtained through the luminance filter are shown in Figure 16. (The night-sky surface brightness μ_{sky} was determined from the night-sky background rate using a photometric zero point $m_0 = 22.7$ appropriate for clear conditions, as described in § 4.6.) In Figure 16a, the large peak results from images obtained under dark conditions, and the long tail (which continues substantially beyond the right-hand edge of the plot) results from images obtained under brighter conditions. In Figure 16b, the prominent peak near $\mu_{\text{sky}} = 21.5 \text{ mag arcsec}^{-2}$ results from images obtained when the Moon is below the horizon, and the prominent peak near $\mu_{\text{sky}} = 18.5 \text{ mag arcsec}^{-2}$ results from images obtained when the full Moon is above the horizon. From Figure 16 it is apparent that under the darkest conditions ever experienced by Condor, the night-sky background rate is $\approx 0.5 e^- s^{-1} \text{pix}^{-1}$ and the night-sky surface brightness is $\mu_{\text{sky}} \approx 21.7 \text{ mag arcsec}^{-2}$ through the luminance filter. The Condor site is as dark as any ground-based astronomical site, including Muana Kea, of which we are aware (see Figure 5 of Barentine 2022). Measurements of the night-sky background rate and night-sky surface brightness through other filters are given in Appendix A.

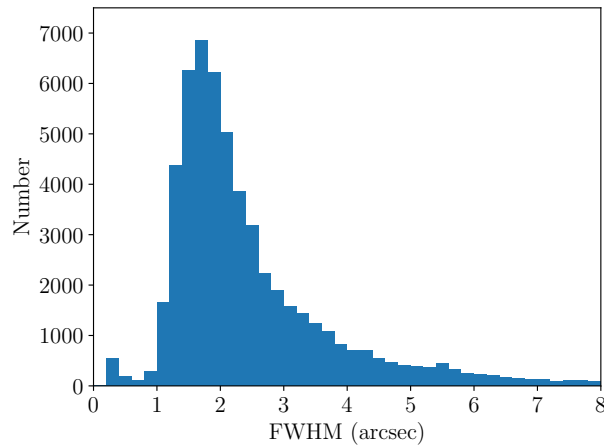


Figure 15. Distribution of “image quality” FWHM (including effects of seeing, focus, and tracking errors) determined from measurements of the autocorrelation function of images obtained through the luminance filter over the time interval stretching from April 21, 2021 through June 19, 2022. The mode of the distribution is 1.6 arcsec, and the median of the distribution is 2.0 arcsec. Bin width is 0.2 arcsec.

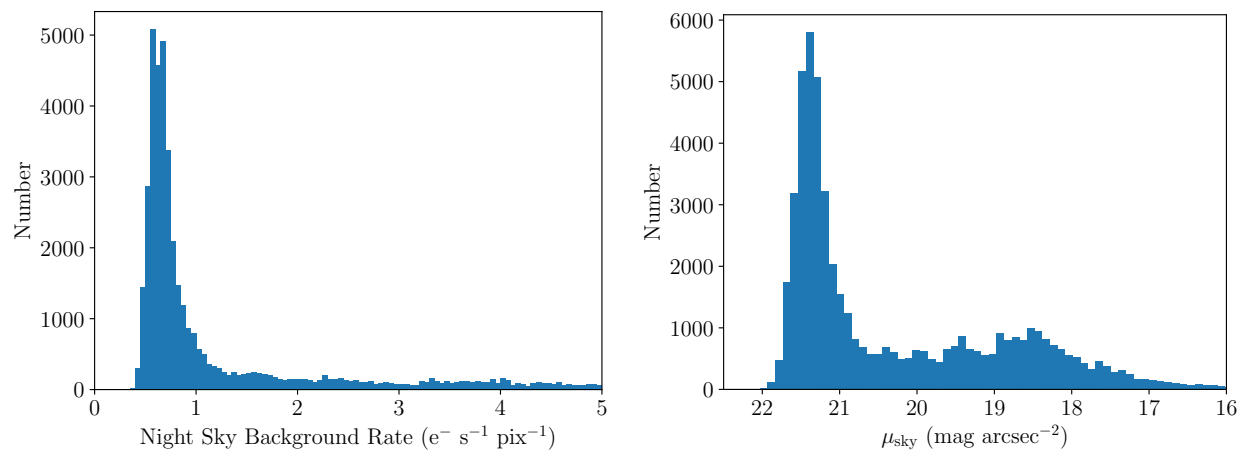


Figure 16. Distribution of night-sky background of a large number of images obtained over a time interval stretching from April 21, 2021 through June 19, 2022 through the luminance filter. The panels show the distribution (*a, left*) in units $e^- s^{-1} \text{pix}^{-1}$ and (*b, right*) in magnitude surface brightness units mag arcsec^{-2} , adopting the photometric calibration described in § 4.6. Bin width of left panel is $0.05 e^- s^{-1} \text{pix}^{-1}$, and bin width of right panel is 0.065 mag.

Over a 60-s exposure, a night-sky background rate of $\approx 0.5 e^- s^{-1} \text{pix}^{-1}$ produces a sky background of $\approx 30 e^-$ per pixel, which corresponds to a sky noise of $\approx 5.5 e^-$ per pixel, which dominates the read noise $1.2 e^-$. We conclude that Condor is sky-noise limited through the luminance filter in 60-s exposures under the darkest conditions it ever experiences. In fact, given the very low read noise of the CMOS detectors, Condor would be sky-noise limited through the luminance filter in exposures as short as 20 or even 10 s (which correspond to sky noises of 3.2 or $2.2 e^-$ per pixel, respectively) under the darkest conditions it ever experiences. Hence if called for by the science case, Condor could operate at a cadence as rapid as 20 or even 10 s through the luminance filter while remaining sky-noise dominated. Condor is easily sky-noise limited through the luminance filter under brighter conditions.

4.9. Sensitivity

The point-source and surface-brightness sensitivities of Condor may be directly determined from the measurements of the CMOS detector read noise described in § 4.1.2, the CMOS detector gain described in § 4.1.3, the plate scale described in § 4.2, the photometric calibration and magnitude zero point described in § 4.6, and the night-sky background rate described in § 4.7. Various point-source and surface-brightness sensitivities are presented in Table 4 as functions of

lunar phase. In Table 4, the point-source sensitivities are 5σ determined for a 60-s exposure summing all six telescopes, assuming optimally-weighted measurements and a seeing FWHM = 1.2 arcsec (and so a PSF FWHM = 1.6 arcsec at $\lambda = 700$ nm, as described in § 4.2) under dark, grey, and bright conditions. And in Table 4, the surface-brightness sensitivities are 3σ determined for exposure times ranging from 1 to 300 h summing all six telescopes averaged over 10×10 arcsec² regions of the sky under dark, grey, and bright conditions. Measurements of the sensitivity through other filters are given in Appendix A.

Table 4: Sensitivity Through Luminance Filter

Lunar Phase	Point Source	Surface Brightness					
	(mag)	Over 10×10 arcsec ²					
	60 s	1 h	3 h	10 h	30 h	100 h	300 h
dark	21.0	28.5	29.1	29.8	30.4	31.0	31.6
grey	20.4	27.8	28.4	29.0	29.6	30.3	30.9
bright	19.7	27.0	27.6	28.3	28.9	29.5	30.1

5. MODE OF OPERATION

In its normal mode of broad-band operation, Condor obtains exposures of exposure time 60 s over dwell times spanning dozens or hundreds of hours. In this way, Condor builds up deep, sensitive images while simultaneously monitoring tens or hundreds of thousands of point sources per field at a cadence of 60 s. In its normal mode of narrow-band operation, Condor obtains exposures of exposure time 600 s. In both cases, random dithers of ≈ 15 arcmin are applied between exposures. Calibration observations are typically interspersed between science observations throughout the course of each night, and images of the dusk and dawn twilight sky are typically obtained every night.

And in its normal mode of operation, Condor operates completely autonomously, controlled only by its control and acquisition computers.

6. SUMMARY AND CONCLUSIONS

The “Condor Array Telescope” or “Condor” is a high-performance “array telescope.” The telescope is comprised of six TEC 180 mm-diameter $f/7$ refracting telescopes, each equipped with (1) an A-P 0.72x QUADTCC-TEC180 four-element telecompressor, (2) A ZWO ASI6200MM monochrome CMOS camera, (3) a ZWO EFW 7/2” seven-position filter wheel, (4) a variety of broad- and narrow-band filters and a diffraction grating, (5) an Optec TCF-Leo low-profile motorized focuser, and (6) and Optec Alnitak motorized remove dust cover. The six telescopes are mounted onto a Planewave L-600 half-for mount with equatorial wedge. Condor is located at a very dark astronomical site in the southwest corner of New Mexico, at the Dark Sky New Mexico observatory. Condor enjoys a wide field of view (2.29×1.53 deg² or 3.50 deg²), is optimized for measuring *both* point sources *and* extended, very low-surface-brightness features, and for broad-band images can operate at a cadence of 60 s (or even less) while remaining sky-noise limited with a duty cycle near 100%. In its normal mode of operation, Condor obtains broad-band exposures of exposure time 60 s over dwell times spanning dozens or hundreds of hours, thereby building up deep, sensitive images while simultaneously monitoring tens or hundreds of thousands of point sources per field at a cadence of 60 s. Given its unique capabilities, Condor can access regions of “astronomical discovery space” that have never before been studied.

We are particularly grateful to Robin Root for providing invaluable assistance and for patiently enduring a planned two-week road trip to New Mexico that turned into a nearly five-month extended stay in New Mexico during the height of the Covid-19 pandemic, which was crucial to the success of the project. We are also particularly grateful to Yuri Petrunin for carefully and meticulously fabricating six superb instruments. We are also grateful to many others who contributed significantly to the project, including Behzad Barzideh, Rich Bersak, Mike Benedetto, Eric Chen, Scott Chrislip, Roland Christen, Kelly Clayton, David Cyrille, John Dey, Jeff Dickerman, Lee Dickerman, Tina Dickerman, Nancy Dipol, Lisette Garcia, Susan Gasparo, John Green, Vicki Grove, Diana Hensley, Michael Hensley, Ciara Lanzetta, Hayley Levine, Barrett Martin, Doreen Nicholas, Daniel Oszust, Celeste Radgowski, Dennis Recla, Teri Sentowski, Sajesh Singh, Michael Smith, Dick Stewart, Zachary Stone, Jonathan Tekverk, Andrew Teresky, Tobias Weiss, George Whitney, and Dave Zurek. This material is based upon work supported by the National Science Foundation under Grants 1910001, 2107954, and 2108234.

Software: astroalign (Beroiz et al. 2020), astropy (Astropy Collaboration et al. 2013, 2018), django (Django Software Foundation 2019), Docker (Merkel 2014), DrizzlePac (Gonzaga et al. 2012), numba (Lam et al. 2015), numpy (Harris et al. 2020), photutils (Bradley et al. 2020), scipy (Virtanen et al. 2020), SExtractor (Bertin & Arnouts 1996b)

APPENDIX

A. PHOTOMETRIC CALIBRATION, NIGHT-SKY BACKGROUND, AND SENSITIVITY THROUGH ALL FILTERS

Most of the observations that have been carried out by Condor so far have been obtained through the luminance filter. But some of the observations have been obtained through the other filters described in § 3.5, particularly the narrow-band filters. Here we present the photometric calibration, night-sky background, and sensitivity of all of the filters described in § 3.5. Because fewer observations have been obtained through filters other than the luminance filters, the various distributions formed from observations through these other filters are subject to larger statistical uncertainties than the corresponding distributions formed from observations through the luminance filter. Accordingly, we consider the values derived here to be representative rather than definitive. These values are nevertheless useful in establishing and documenting the capabilities of Condor.

We determined photometric calibrations and magnitude zero points through all filters using methods similar to those described in § 4.6. We determined night-sky background rate and night-sky surface brightness of all filters using methods similar to those describe in § 4.8. And we determined sensitivities through all filters using methods similar to those described in § 4.9. The photometric calibrations, magnitude zero points, night-sky background rates, and night-sky surface brightnesses of all filters are presented in Table 5, and the sensitivities of all filters are presented in Table 6.

Table 5: Photometric Calibration and Night-Sky Background Through All Filters

Filter	Telescope	Photometric Calibration		Night-Sky Background	
		($\mu\text{Jy ADU}^{-1} \text{ s}$)	m_0	Rate ($\text{e}^- \text{ s}^{-1} \text{ pix}^{-1}$)	μ_{sky} (mag arcsec^{-2})
luminance	4	3.5	22.7	0.5	21.7
Sloan g'	0	11	21.3	0.5	21.5
Sloan r'	2	9.5	21.6	0.4	20.9
Sloan i'	4	15	21.0	0.3	21.0
He II 468.6 nm	0	250	18.0	0.02	21.4
[O III] 500.7 nm	1	300	17.8	0.02	21.3
He I 587.5 nm	2	250	18.1	0.02	20.8
H α 656.3 nm	3	450	17.4	0.02	20.8
[N II] 658.4 nm	4	400	17.4	0.02	21.0
[S II] 671.6 nm	5	450	17.4	0.02	21.1

NOTE—Here “telescope” refers to telescope used to make measurements.

Table 6: Sensitivity Through All Filters

Filter	Lunar Phase	Point Source	Surface Brightness					
		(mag)	Over 10×10 arcsec ² (mag arcsec ⁻²)					
		60 s	1 h	3 h	10 h	30 h	100 h	300 h
luminance	dark	21.0	28.5	29.1	29.8	30.4	30.8	31.6
	grey	20.4	27.8	28.4	29.0	29.6	30.3	30.9
	bright	19.7	27.0	27.6	28.3	28.9	29.5	30.1
Sloan g'	dark	19.6	27.1	27.7	28.4	29.0	29.6	30.2
	grey	19.0	26.4	27.0	27.6	28.2	28.9	29.5
	bright	18.3	25.6	26.2	26.9	27.5	28.1	28.7
Sloan r'	dark	20.0	27.5	28.1	28.8	29.4	30.0	30.6
	grey	19.4	26.8	27.4	28.0	28.6	29.3	29.9
	bright	18.7	26.0	26.6	27.3	27.9	28.5	29.1
Sloan i'	dark	19.5	27.1	27.7	28.3	28.9	29.6	30.2
	grey	18.9	26.3	26.9	27.6	28.2	28.8	29.4
	bright	18.3	25.6	26.2	26.8	27.4	28.1	28.7
He II 468.6 nm	dark	17.2	25.5	26.1	26.8	27.3	28.0	28.6
	grey	16.9	24.8	25.4	26.0	26.6	27.3	27.9
	bright	16.5	24.1	24.7	25.3	25.9	26.6	27.2
[O III] 500.7 nm	dark	17.0	25.3	25.9	26.6	27.1	27.8	28.4
	grey	16.7	24.6	25.2	25.8	26.4	27.1	27.7
	bright	16.3	23.9	24.5	25.1	25.7	26.4	27.0
He I 587.5 nm	dark	17.3	25.6	26.2	26.9	27.4	28.1	28.7
	grey	17.0	24.9	25.5	26.1	26.7	27.4	28.0
	bright	16.6	24.2	24.8	25.4	26.0	26.7	27.3
H α 656.3 nm	dark	16.6	24.9	25.5	26.2	26.7	27.4	28.0
	grey	16.3	24.2	24.8	25.4	26.0	26.7	27.3
	bright	15.9	23.5	24.1	24.7	25.3	26.0	26.6
[N II] 658.4 nm	dark	16.6	24.9	25.5	26.2	26.7	27.4	28.0
	grey	16.3	24.2	24.8	25.4	26.0	26.7	27.3
	bright	15.9	23.5	24.1	24.7	25.3	26.0	26.6
[S II] 671.6 nm	dark	16.6	24.9	25.5	26.2	26.7	27.4	28.0
	grey	16.3	24.2	24.8	25.4	26.0	26.7	27.3
	bright	15.9	23.5	24.1	24.7	25.3	26.0	26.6

NOTE—Point-source sensitivities are 5σ summing all six telescopes assuming optimally-weighted measurements and a seeing FWHM = 1.2 arcsec. Surface-brightness sensitivities are 3σ summing all six telescopes averaged over 10×10 arcsec² regions of the sky.

REFERENCES

- Abraham, R. G., & van Dokkum, P. G. 2014, *PASP*, 126, 55
- Astropy Collaboration, Robitaille, T. P., Tollerud, E. J., et al. 2013, *A&A*, 558, A33, doi: [10.1051/0004-6361/201322068](https://doi.org/10.1051/0004-6361/201322068)
- Astropy Collaboration, Price-Whelan, A. M., Sipőcz, B. M., et al. 2018, *AJ*, 156, 123, doi: [10.3847/1538-3881/aabc4f](https://doi.org/10.3847/1538-3881/aabc4f)
- Barentine, J. C. 2022, arXiv e-prints, arXiv:2207.03551. <https://arxiv.org/abs/2207.03551>
- Beroiz, M., Cabral, J., & Sanchez, B. 2020, *Astronomy and Computing*, 32, 100384, doi: <https://doi.org/10.1016/j.ascom.2020.100384>
- Bertin, E., & Arnouts, S. 1996a, *A&AS*, 117, 393, doi: [10.1051/aas:1996164](https://doi.org/10.1051/aas:1996164)
- . 1996b, *A&AS*, 117, 393, doi: [10.1051/aas:1996164](https://doi.org/10.1051/aas:1996164)
- Bradley, L., Sipőcz, B., Robitaille, T., et al. 2020, *astropy/photutils*: 1.0.0, 1.0.0, Zenodo, doi: [10.5281/zenodo.4044744](https://doi.org/10.5281/zenodo.4044744)
- Calabretta, M. R., & Greisen, E. W. 2002, *A&A*, 395, 1077, doi: [10.1051/0004-6361:20021327](https://doi.org/10.1051/0004-6361:20021327)
- Chao, C. Y.-P., Yeh, S.-F., Wu, M.-H., et al. 2019, *Sensors*, 19, doi: [10.3390/s19245447](https://doi.org/10.3390/s19245447)
- Django Software Foundation. 2019, *Django*, 2.2.1. <https://djangoproject.com>
- Gaia Collaboration, Clementini, G., Eyer, L., et al. 2017, *A&A*, 605, A79, doi: [10.1051/0004-6361/201629925](https://doi.org/10.1051/0004-6361/201629925)
- Gaia Collaboration, Brown, A. G. A., Vallenari, A., et al. 2018, *A&A*, 616, A1, doi: [10.1051/0004-6361/201833051](https://doi.org/10.1051/0004-6361/201833051)
- . 2021, *A&A*, 649, A1, doi: [10.1051/0004-6361/202039657](https://doi.org/10.1051/0004-6361/202039657)
- Gander, F. F., Maillard, J., Zerlang, L., et al. 1931, *The Condor*, 33, 73. <http://www.jstor.org/stable/1363313>
- Gilhuly, C., Merritt, A., Abraham, R., et al. 2022, *The Astrophysical Journal*, 932, 44, doi: [10.3847/1538-4357/ac6750](https://doi.org/10.3847/1538-4357/ac6750)
- Gonzaga, S., Hack, W., Fruchter, A., & Mack, J. e. 2012, *The DrizzlePac Handbook*, STScI, Baltimore, MD
- Haffner, L. M., Reynolds, R. J., Madsen, G. J., et al. 2011, *ASP Conf. Ser.*, 438, 388. <https://arxiv.org/abs/1104.2427>
- Harris, C. R., Millman, K. J., van der Walt, S. J., et al. 2020, *Nature*, 585, 357, doi: [10.1038/s41586-020-2649-2](https://doi.org/10.1038/s41586-020-2649-2)
- Harwit, M. 1984, *Cosmic Discovery* (MIT Press)
- Karpov, S., Bajat, A., Christov, A., Prouza, M., & Beskin, G. 2021, arXiv e-prints, arXiv:2101.01517. <https://arxiv.org/abs/2101.01517>
- Kavaldjiev, D., & Ninkov, Z. 2001, *Optical Engineering*, 40, 162
- Klypin, A., Kravtsov, A., Valenzuela, O., & Prada, F. 1999, *ApJ*, 522, 82
- Lam, S. K., Pitrou, A., & Seibert, S. 2015, in *Proceedings of the Second Workshop on the LLVM Compiler Infrastructure in HPC*, 1–6
- Law, N., Corbett, H., Galliher, N., et al. 2022, *Publications of the Astronomical Society of the Pacific*, 134, doi: [10.1088/1538-3873/ac4811](https://doi.org/10.1088/1538-3873/ac4811)
- Liu, Q., Abraham, R., Gilhuly, C., et al. 2022, *ApJ*, 925, 219, doi: [10.3847/1538-4357/ac32c6](https://doi.org/10.3847/1538-4357/ac32c6)
- Merkel, D. 2014, *Linux journal*, 2014, 2
- Merritt, A., Pillepich, A., van Dokkum, P., et al. 2020, *MNRAS*, 495, 4570, doi: [10.1093/mnras/staa1164](https://doi.org/10.1093/mnras/staa1164)
- Merritt, A., van Dokkum, P., & Abraham, R. 2014, *ApJ*, 787, L37, doi: [10.1088/2041-8205/787/2/L37](https://doi.org/10.1088/2041-8205/787/2/L37)
- Merritt, A., van Dokkum, P., Abraham, R., & Zhang, J. 2016a, *ApJ*, 830, 62, doi: [10.3847/0004-637X/830/2/62](https://doi.org/10.3847/0004-637X/830/2/62)
- Merritt, A., van Dokkum, P., Danieli, S., et al. 2016b, *ApJ*, 833, 168, doi: [10.3847/1538-4357/833/2/168](https://doi.org/10.3847/1538-4357/833/2/168)
- Ofek, E. O., & Ben-Ami, S. 2020, *PASP*, 132, 125004, doi: [10.1088/1538-3873/abc14c](https://doi.org/10.1088/1538-3873/abc14c)
- Paillassa, M., Bertin, E., & Bouy, H. 2020, *A&A*, 634, A48, doi: [10.1051/0004-6361/201936345](https://doi.org/10.1051/0004-6361/201936345)
- Rousseau-Nepton, L., Martin, R. P., Robert, C., et al. 2019, *MNRAS*, 489, 5530, doi: [10.1093/mnras/stz2455](https://doi.org/10.1093/mnras/stz2455)
- Spitler, L. R., Longbottom, F. D., Alvarado-Montes, J. A., et al. 2019, *The Huntsman Telescope*. <https://arxiv.org/abs/1911.11579>
- van Dokkum, P. G., Abraham, R., & Merritt, A. 2014, *ApJ*, 782, L24, doi: [10.1088/2041-8205/782/2/L24](https://doi.org/10.1088/2041-8205/782/2/L24)
- Virtanen, P., Gommers, R., Oliphant, T. E., et al. 2020, *Nature Methods*, 17, 261, doi: [10.1038/s41592-019-0686-2](https://doi.org/10.1038/s41592-019-0686-2)
- Wright, N. J. 2016, in *The Universe of Digital Sky Surveys*, ed. N. R. Napolitano, G. Longo, M. Marconi, M. Paolillo, & E. Iodice, Vol. 42, 55, doi: [10.1007/978-3-319-19330-4_7](https://doi.org/10.1007/978-3-319-19330-4_7)